An NMR-compatible microfluidic platform enabling *in situ* electrochemistry

Hossein Davoodi, Nurdiana Nordin, Lorenzo Bordonali, Jan G. Korvink, Neil MacKinnon, and Vlad Badilita

Electronic Supplementary Information

S1 Micro-fabrication process of the inserts

As presented in Section 2.3, different electrode configurations were introduced starting from the basic microfluidic channel structure. The microfluidic channel was fabricated on a 4-inch MEMpax substrate by spincoating 90 μm SU-8 followed by UV-lithography (EVG®620 EV Group) to define the channel structure. 5 μm SU-8, being spincoated on the second MEMpax wafer, served as the adhesion layer between the two MEMpax wafers which were further bonded using a compression bonding machine (EVG®510 EV Group). The assembly was subjected to UV exposure (300 mJ/cm^2) and baked (4 h at 95 °C) to enhance the mechanical and chemical stability of the bond. The inlet and outlet of the microfluidic channel were drilled on the top glass wafer using a nanosecond laser (PIRANHA® ACSYS). The assembly was diced into the individual chips using the same laser.

The planar electrodes were fabricated with the same channel height, substrate, and cap layer as the insert with no electrodes. The fabrication process was modified in order to integrate the metallic structures into the chips depending on the required total thickness. The working electrodes were patterned out of 2/1 nm and 24/10 nm thick evaporated gold/chromium layers. Other structures such as the access tracks, pads, and counter electrodes were realised using a 5 μm thick electroplated gold layer. In the first step, the substrate was covered with the Cr/Au seed layer. A mould for electroplating was then defined using SU-8 photoresist and UV-lithography followed by gold electroplating. In the next step, the mould was stripped and an SU-8 cover layer for the working electrodes was spincoated and patterned using UV-lithography. The unprotected seed layer was etched and the cover layer was stripped. The channel structures were further processed in an identical manner as for the electrode-free insert to form the channel and bond it to the top layer. The fabrication process is schematically illustrated in Figure S1a.

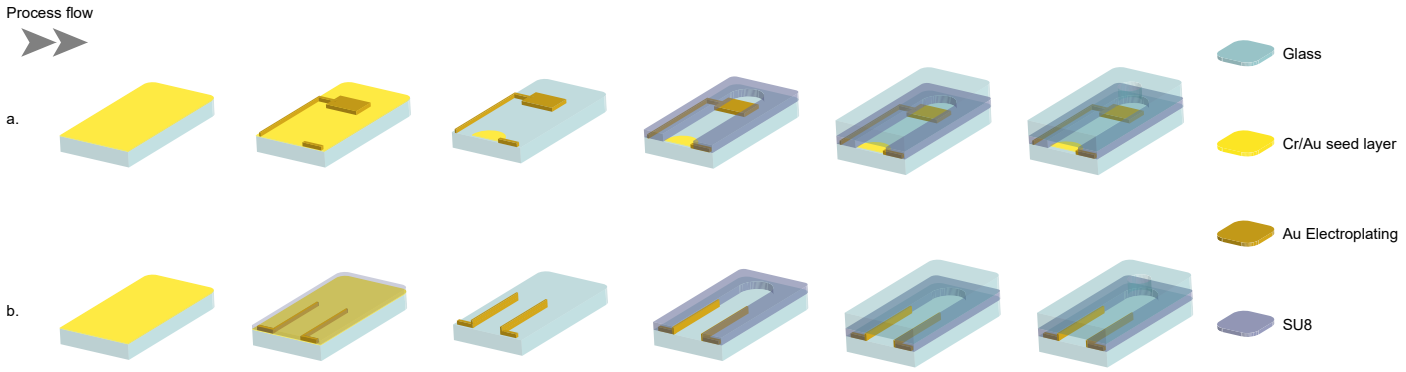

Fig. S1 (a) The inserts with planar electrodes are fabricated by electroplating the counter electrode on the seed layer, developing active electrode through the seed layer, patterning the channel, bonding the top glass, and drilling in-/outlets. (b) The inserts, having active electrodes as the sidewalls, are fabricated by electroplating the planar electrodes and sidewalls, patterning the channel, bonding the top glass, and drilling the in-/outlet.

Sidewall-electrode inserts were fabricated in a similar way as the electrode-free insert, except for two intermediate metallisation steps to introduce the sidewalls, as well as the connecting tracks and the contact pads. For this purpose, the substrate was covered with a Cr/Au seed layer (20/60 nm). For the first mould, an SU-8 layer was patterned on the substrate followed by 5 μm gold electroplating in order to define the tracks and the contact pads. In the next step, a second mould was formed on top of the first layer using SU-8 for the total height of 90 μm in order to define the sidewall electrodes. The sidewall electrodes were electroplated for the desired height of 80 μm (30 μm width). The mould structures were stripped followed by seed layer etching. A 90 μm thick SU-8 was spincoated for both encapsulation of the electrodes and structuring the microfluidic channel. The rest of the process was the same as the electrode-free insert. The process is depicted in Figure S1b.

S2 Characterisation of the fabricated electrodes

S2.1 Profile measurements

Figure S2 demonstrates white-light interferometery and scanning electron microscopy (SEM) measurements evaluating profile of different fabricated electrodes.

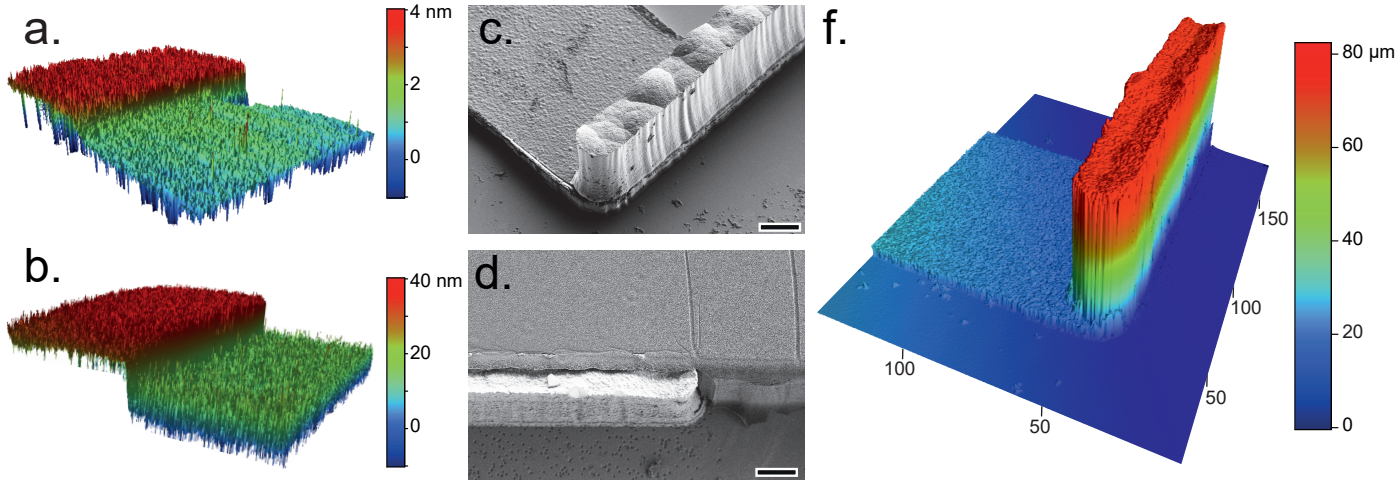

Fig. S2 Electrodes geometry: (a) Profile of the 3 nm-thick planar electrode, measured using white-light interferometer, shows two steps corresponding to chromium and gold PVD layers; (b) Profile of the 34 nm-thick planar electrode, measured using white-light interferometer, shows two steps corresponding to chromium and gold PVD layers; (c) SEM image of a sidewall electrode and its corresponding track fabricated by gold electroplating; (d) SEM image of a sidewall electrode encapsulated by SU-8, forming the channel; (e) Profile of a sidewall electrode and its corresponding track, measured using white-light interferometer.

S2.2 Conductivity of the planar electrodes

The electrode thickness and sheet resistance of the planar electrodes (3 nm- and 34 nm-thick) are summarised in Table S1. Additionally, the atomic content of the substrate coated with chromium and gold is evaluated with Scanning Electron Microscopy / Energy Dispersive X-Ray Spectroscopy (SEM/EDX). Since the electron interaction depth is $\sim 2\,\mu$m the absolute content of the chromium and gold is low however the comparison of these values correlates with the sheet resistance and layer thickness measured using white-light interferometer.

Table S1 Comparison of different planar electrodes.

Sample	Nominal Cr thickness (nm)	Nominal Au thickness (nm)	Experimental thickness (nm)	Experimental sheet resistance ($\Omega/\square$)	Cr atomic content (%)	Au atomic content (%)
34 nm	10	24	33	1.0 ± 0.1	2.38 ± 0.10	4.75 ± 0.10
3 nm	1	2	3.5	72 ± 20	0.12 ± 0.03	0.20 ± 0.04

S3 B_1 field distribution at the sample region

Distribution of B_1 field at different applied powers and for different electrode geometries is illustrated in Figure S3.

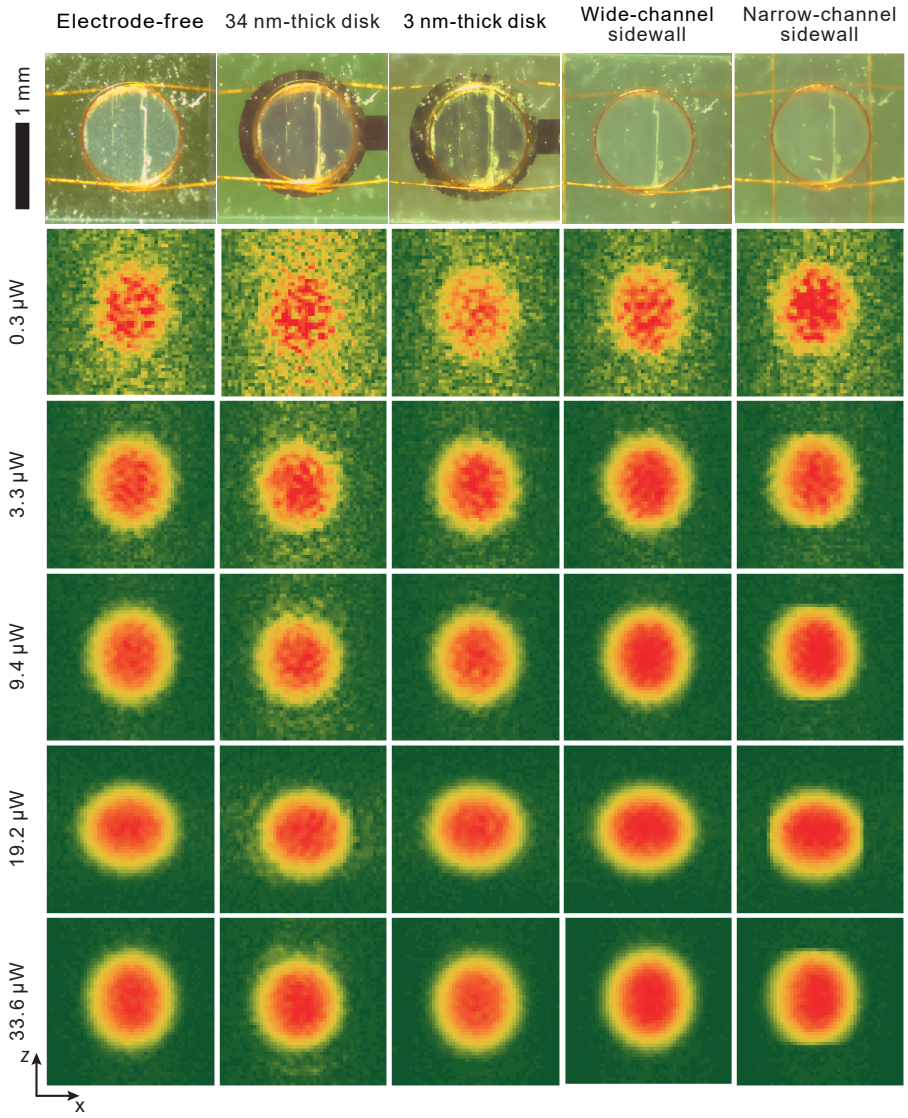

Fig. S3 Distribution of the B_1 field at the sample volume at different flip angles corresponding to a range of excitation powers. The asymmetric distribution in the x- and z-axis of the colour maps is due to the relative direction of the B_0 and B_1 fields: the B_0 field is oriented along the z-axis, therefore the B_1 components along this direction, i.e., parallel to B_0, do not produce any signal.

S4 Analysis of 34 nm-thick electrode performance

According to the nutation signal presented in Figure 2, two differences are observed between the simulation and measurement results of the 34 nm-thick planar electrode:

- A_{450}/A_{90} parameter extracted from the measurement is half of that predicted by simulation. Figure S4 illustrates the B_0 and B_1 field distributions collected from simulations and measurements. The simulation results have been collected for a plane parallel to the electrode surface and at the middle height of the channel whereas the measurement results were collected from a slice parallel to the electrode and slice thickness equal to the channel height. Therefore, the measurement is integral over the channel height.

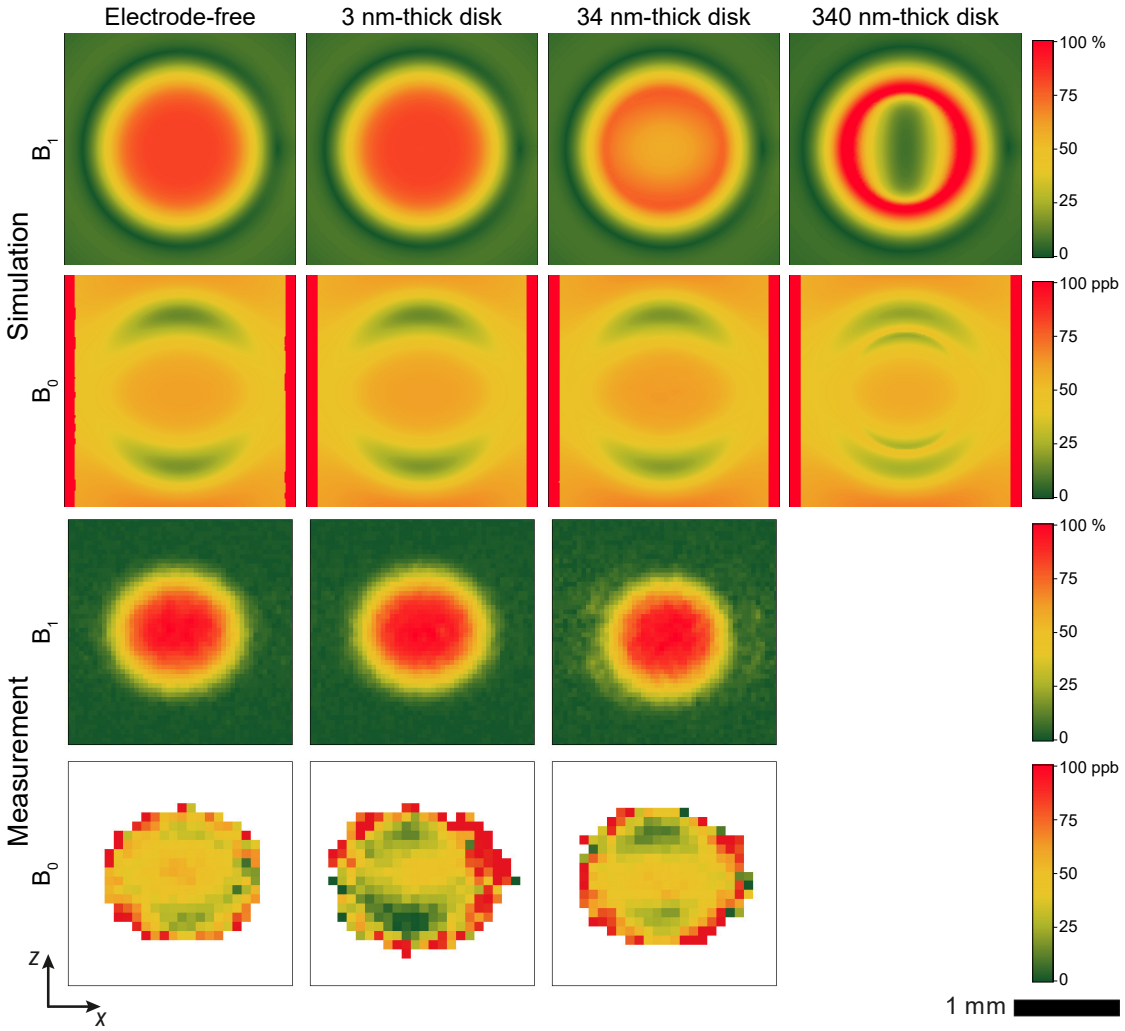

Fig. S4 B_1 and B_0 field distributions predicted by simulations and measured using MRI for different geometries. Presence of the planar electrode depletes the field from the centre, and accumulates it at the edges. This effect increases with electrode-thickness. The simulation results reveal that the main B_0 distortion source is the coil windings. However the 340 nm electrode also introduces susceptibility perturbations. Presence of the chromium seed layer is degrading the measurement results even for 3 nm and 34 nm-thick layers.

According to the simulation results, by increasing the electrode thickness, B_1 field is depleted from the center of the electrode and focused at its edges to circumvent the metallic structure. B_0 simulations show distortions in the form of a pair of round brackets, which are introduced by the coil windings. By increasing the electrode thickness, a new pair of round brackets is introduced, which corresponds to the electrode edges. For 3 nm- and 34 nm electrode thickness, the effect of electrode is negligible comparing to the coil distortions. The NMR signal depends on the relative distribution of both B_0 and B_1. As discussed in Table 1, the NMR spectrum corresponding to the 34 nthem-thick electrode is considerably broader than the spectra corresponding to the 3 nm-thick electrode and electrode-free cases since B_1 is more intense around the edges, where B_0 is distorted. The 340 nm-thick electrode exhibits further

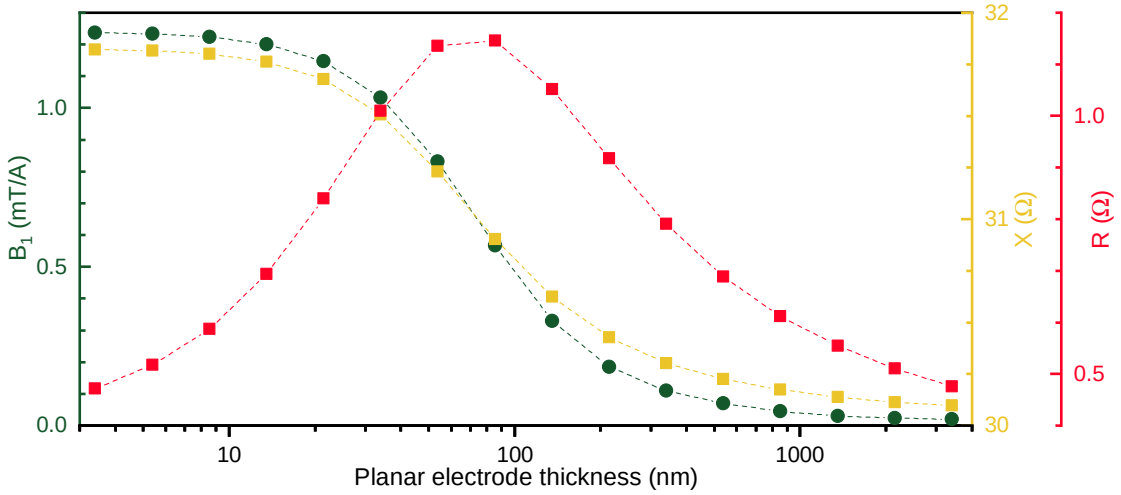

Fig. S5 B_1 field amplitude at the isocenter of the assembly and impedance of the coil as a function of electrode thickness obtained from simulation results.

line-broadening as a result of the secondary B_0 distortions, caused by the electrode, as well as a higher concentration of B_1 at the distorted regions.

In the measurement results, the perturbation of B_1 field for 34 nm-thick electrode is obvious as the field is extended in x-direction. Besides, the lower SNR of the image corresponds to the lower maximum field intensity. Differences between the measured patterns and the simulated patterns are attributed to the integration of the pixels in slice thickness (y-direction). B_0 measurements show round bracket perturbations of the field similar to the predictions. The perturbation increases with the layer thickness and it is obvious even for 3 nm- and 34 nm-thick electrodes. This observation is attributed to the presence of chromium seed layer which has been ignored in the simulations. The magnetic susceptibility value of chromium is 320 ppm, whereas for gold the susceptibility value is -34 ppm.[1] Considering these facts, the NMR signal is more distorted in 34 nm-thick electrode and and this extremely localised distortion cannot be fully compensated by shimming. These distortions are more weighted in higher flip angles and therefore the nutation signal suffers from B_0 inhomogeneities. This effect is assumed to be the main reason behind the faster decay of the nutation experiment in comparison to the simulated nutation signal.

- Unlike other geometries, the nutation frequency in the simulated case is lower than that of measurements. This difference is attributed to the power dissipation in the electrode and the decoupling of the Helmholtz pair as a result of the electrode presence. As presented in Figure S5, there is a critical thickness of the electrode at which the resistance of the coil is maximised. This suggests that the power dissipation in the electrode is maximum for that thickness. In the experimental case, the electrode consists of 24 nm gold and 10 nm chromium, whereas in the simulation, the electrode is assumed to be a 34 nm-thick gold layer. Since the chromium conductivity is smaller than the conductivity of gold and therefore its skin depth is higher, the power dissipation in the electrode for the experimental case is less and the nutation experiment has a higher frequency.

References

1 J. F. Schenck, *Medical Physics*, 1996, **23**, 815–850.